

Assessment of point and line contact stiffness formulations leading to the initiation of hammering type brake squeal

Osman Taha Sen^{a)} and Rajendra Singh^{b)}

(Received: 25 April 2020; Revised: 13 October 2020; Accepted: 14 December 2020)

This article proposes a refined nonlinear mathematical model to conceptually investigate the brake pad kinematics and dynamics in order to reveal certain important aspects that have been ignored in prior studies. In particular, the proposed model is formulated as a three degree-of-freedom mass positioned on a rigid frictional surface moving at constant velocity. The mass is assumed to make planar motion in vertical plane, two translations and one rotation. The interfacial contact is first examined by a point contact model with linear translational springs at edges and then the line contact is defined over the entire interface. Furthermore, kinematic and clearance nonlinearities are included. The nonlinear governing equations with point contacts at edges are numerically solved at certain angular arrangements of normal force vectors. Then, the line contact interface is solved again for the same normal force vector arrangements. Comparison reveals that the line contact approach provides more meaningful results. Finally, a linearized system model and the existence of quasi-static sliding motion are examined over a range of the normal force vector arrangements. Overall, inclusion of the rotational degree of freedom in the source model is crucial and the importance of pad-disc separation is clearly explained by the proposed formulation. This leads to a better understanding of the hammering type brake squeal source mechanisms while overcoming the limitation of prior minimal order models. © 2021 Institute of Noise Control Engineering.

Primary subject classification: 11.8.1; Secondary subject classification: 41.5

1 INTRODUCTION

Brake squeal is a friction-induced high-frequency noise problem (beyond 1 kHz) that is observed in automotive brake systems. There is a significant body of literature on the brake squeal when compared to other brake noise problems, as evident from two exhaustive reviews^{1,2}. Even though several physical mechanisms have been proposed for squeal initiation¹, no practical solutions could be offered at the design stage. This phenomenon is regarded as a dynamic stability problem, which is usually linked to the flutter instability mechanism caused by non-conservative forces emerging at the contact interface³. Consequently, the modeling of the contact stiffness between brake disc and pad is crucial for the investigation of brake squeal initiation⁴⁻⁶.

In one particular study by Hamabe et al.⁷, the brake squeal phenomenon is studied with a two degree of freedom linear system, where the brake pad/disc contact

interface is described by a linear stiffness term. This model by Hamabe et al.⁷ is then extended by Hoffmann et al.⁸ with a single point contact model while keeping the degree of freedom of their nonlinear model intact. However, kinematic nonlinearities arising due to the normal force vector arrangements and surface separation effects are both ignored in the prior work^{7,8}. Both of these important aspects are considered in this article. The chief goal of this article is (a) to examine the role of point and line contact models via a three degree-of-freedom mechanical system model and (b) examine the role of brake pad rotational dynamics on the initiation of brake squeal noise through the hammering mechanism since it has not been adequately investigated by prior minimal order models¹⁻¹⁶. An experimental validation is beyond the scope for this article, although suggestions will be offered for a future inquiry.

2 LITERATURE REVIEW

The literature on the contact interface models is limited when compared to the body of papers on the brake squeal. In general, the following two approaches have been adopted to model the contact interface: (a) low dimensional models with single contact points (mostly

^{a)} Istanbul Technical University, Department of Mechanical Engineering, Istanbul, TURKEY; email: senos@itu.edu.tr.

^{b)} The Ohio State University, Department of Mechanical and Aerospace Engineering, Columbus, OH, USA; email: singh.3@osu.edu.

nonlinear)^{8–11}, and (b) higher dimensional models (mostly linear) with elastic regime defined over the interfacial surface^{12–15}. For instance, Massi et al.¹⁶ numerically investigated the squeal problem with both linear and nonlinear system approaches. The linear system approach consists of finite element model of a particular experiment, and modal characteristics are obtained through the complex eigenvalue solution. In the nonlinear system approach, the elastic interface is defined over a surface, and subsequently, time domain solutions are acquired to simulate the squeal phenomenon. Furthermore, the study¹⁶ revealed that detachment at the contact interface is inevitable at least over a portion of the entire interface due to the elastic deformations of mating surfaces. During a squeal event, excitation of the system at one of its resonant frequencies increases these deformations, thereby significantly changing the contact area. Renaud et al.¹⁷ measured the dynamic motion of the pad with six tri-axial accelerometers from the backing plate of the piston side pad. They observed that the pad motion plays a significant role in squeal initiation and squeal noise emerges only when the super-harmonics of the fundamental frequency are excited. The squeal frequencies were found to be dependent on the brake pressure, and operational deflection motions of the pad motion was a combination of bending and torsional modes dominantly at the leading edge of the pad during the squeal event.

Elmaian et al.¹⁸ developed a phenomenological lower dimensional model that allowed the simulation of stick-slip, sprag-slip and mode-coupling phenomena. They classified the underlying noise problems based on the occurrence of slip, stick and separation regimes (contact states), and the contact between mating surfaces was defined as a point contact. For example, the squeak type problem was classified with successive stick and slip regimes, but all three regimes are observed in both squeal and squeak type phenomena. In an interesting study by Oura et al.¹⁹, two different contact formulations were investigated with mathematical models of dimension three. The first formulation is essentially a pin-on-disc model where the contact in between is defined at a single point. In the second formulation, the contact is defined over a surface at the interface; hence, the contact stiffness is distributed over an area (instead of lumping it at a point as in the first model). Furthermore, they attributed squeal initiation to the pressure dependency of the contact stiffness. Sen et al.²⁰ investigated the squeal phenomenon with a nonlinear two degree-of-freedom mathematical model, where the brake pad and disc contact interface is defined at a single point. The stability of the system was examined through a linearized model, and time domain solutions are obtained through the numerical solution of nonlinear governing equations. Results showed a contradiction leading to the inadequacy for the linearized stability analyses.

Furthermore, time domain solutions failed to reveal the differences between system dynamics under certain operational characteristics, which could be attributed to the simplified single point contact formulation.

The hammering behavior has been defined as the rocking action of brake pads while they slide over the disc surface²¹. Therefore, an investigation of the angular motions of brake pad becomes crucial. In yet another article, the sprag-slip action has been proposed as a source mechanism²². Since the sprag-slip is the motion of brake pad exhibiting consecutive jumps on the disc surface, it may not be related to the pad's rotational dynamics. As first proposed by Spurr²², the sprag-slip behavior as a squeal mechanism may develop at a friction interface depending on the kinematics of the system, i.e., due to the geometry of the brake assembly, excessive amount of friction force develops and the system deforms elastically. This deformation then leads to a reduction in the friction force, until the surfaces in contact stick again. In the stiction regime, the friction force again starts to increase, and the system returns to its initial state, thereby developing a cyclic behavior²². Sinou et al.²³ have investigated the sprag-slip mechanism via a three degree-of-freedom mechanical model with elastic nonlinearities. Their parametric analysis suggests that the system may exhibit unstable behavior even with a constant friction coefficient. Furthermore, their theoretical approach provides satisfactory results when compared with experiments. Hoffmann and Gaul²⁴ studied the sprag-slip problem as well by using lower dimensional mathematical models and show conditions under which sprag-slip oscillations could be triggered. They introduced a pin-on-disc system model where the axial and bending motions of the pin are considered. Furthermore, Hoffmann and Gaul²⁴ have found that the system may not have any static solution at certain values of the friction coefficient and/or the inclination angle of the pin with respect to the disc surface; i.e., no steady sliding state might exist.

3 THREE DEGREE-OF-FREEDOM NONLINEAR SQUEAL MODEL

A minimal dimension model as a representation of disc brake squeal source is formulated while focusing on the leading/trailing edge dynamics of the brake pad. As shown in Fig. 1, a three degree-of-freedom mass sliding on a rigid frictional surface and the contact in between the mass and the sliding surface defined with two alternate models. In the first contact stiffness formulation (B1), two discrete springs are defined at the leading and trailing edges of the mass where the interfacial contact stiffnesses are represented with two linear springs (Fig. 1). In the second formulation (B2 as depicted in Fig. 2), a line contact over the entire contact interface is proposed, and now the contact

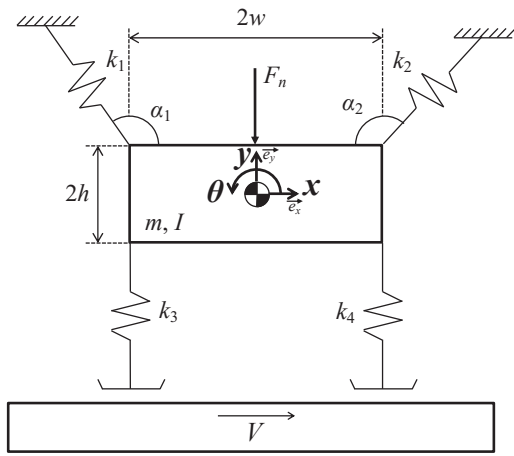


Fig. 1—Three degree-of-freedom nonlinear mechanical system with point contacts (lumped springs) at the leading and trailing edges (model B1).

stiffness is assumed to be linear and evenly distributed over the contact line. Furthermore, the three degree-of-freedom on the mass is defined with two translations ($x(t)$ and $y(t)$) and one rotation ($\theta(t)$); i.e., the mass is assumed to do planar motion on the \vec{e}_x - \vec{e}_y vertical plane. Hence, the mass is an inertial element with geometric dimensions ($2h$ and $2w$). As displayed in Figs. 1 and 2, the mass (m, I) is attached to common ground with two linear springs (k_1 and k_2) at two arbitrary angles (α_1 and α_2). Note that these angles (α_1 and α_2) define the configuration of normal force vectors. Furthermore, the pad is positioned over a rigid frictional surface translating at a constant speed V , and the force F_n is defined as a preload on the mass to represent the actuation (brake) force effect. The specific objectives of the current study are as follows with the Coulomb friction assumption; an experimental validation is beyond the scope.

1. Develop a discrete contact stiffness model at the leading and trailing edges of the contact interface (model B1) and numerically solve the nonlinear governing equations at several normal force vector configurations.
2. Propose a line contact (distributed stiffness) model over the entire contact interface (model B2) and compare the results of point and line contact models for the same angular arrangements of the normal force vectors.
3. Simplify the nonlinear governing equations by ignoring clearance nonlinearity and linearizing the nonlinear terms due to kinematics to generate a linearized model (model B3), and investigate the existence of quasi-static sliding motion over a range of normal force vector arrangements.

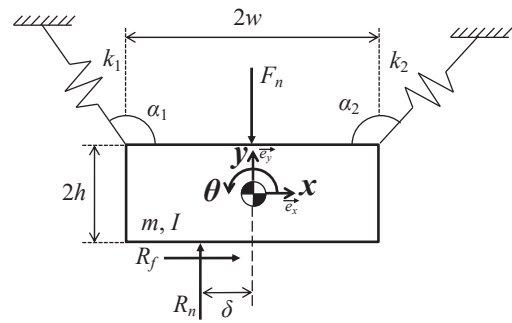


Fig. 2—Three degree-of-freedom nonlinear mechanical system with the line contact (distributed stiffness) interface formulation as defined by the interfacial forces R_n and R_f (model B2).

4 FORMULATION WITH POINT CONTACTS AT EDGES (MODEL B1)

Two contact interfaces of the model depicted in Fig. 1 are defined at the leading and trailing edges of the mass with lumped linear springs k_3 and k_4 , respectively. Both springs are assumed to be unidirectional; i.e., restoring forces in springs k_3 and k_4 can only be developed under compression. The governing equations of the system of Fig. 1 are derived by first defining the elastic force vectors acting upon the mass which require the position vectors of the fixed ($\vec{r}_{f,i}$) and free (\vec{r}_i) ends of each spring. The position vectors for the fixed ends ($\vec{r}_{f,i}$) of all springs are derived as follows:

$$\vec{r}_{f,1} = [x_0 - d \cos(\beta - \theta_0) + L_1 \cos(\alpha_1)] \vec{e}_x + [y_0 + d \sin(\beta - \theta_0) + L_1 \sin(\alpha_1)] \vec{e}_y, \quad (1a)$$

$$\vec{r}_{f,2} = [x_0 + d \cos(\beta + \theta_0) - L_2 \cos(\alpha_2)] \vec{e}_x + [y_0 + d \sin(\beta + \theta_0) + L_2 \sin(\alpha_2)] \vec{e}_y, \quad (1b)$$

$$\vec{r}_{f,3} = [x_0 + x - d \cos(\beta + \theta_0 + \theta)] \vec{e}_x + [y_0 - d \sin(\beta + \theta_0) - L_3] \vec{e}_y, \quad (1c)$$

$$\vec{r}_{f,4} = [x_0 + x + d \cos(\beta - \theta_0 - \theta)] \vec{e}_x + [y_0 - d \sin(\beta - \theta_0) - L_4] \vec{e}_y. \quad (1d)$$

Similarly, the position vectors for the free ends (\vec{r}_i) are obtained as:

$$\vec{r}_1 = [x_0 + x - d \cos(\beta - \theta_0 - \theta)] \vec{e}_x + [y_0 + y + d \sin(\beta - \theta_0 - \theta)] \vec{e}_y, \quad (2a)$$

$$\vec{r}_2 = [x_0 + x + d \cos(\beta + \theta_0 + \theta)]\vec{e}_x + [y_0 + y + d \sin(\beta + \theta_0 + \theta)]\vec{e}_y, \quad (2b)$$

$$\vec{r}_3 = [x_0 + x - d \cos(\beta + \theta_0 + \theta)]\vec{e}_x + [y_0 + y - d \sin(\beta + \theta_0 + \theta)]\vec{e}_y, \quad (2c)$$

$$\vec{r}_4 = [x_0 + x + d \cos(\beta - \theta_0 - \theta)]\vec{e}_x + [y_0 + y - d \sin(\beta - \theta_0 - \theta)]\vec{e}_y. \quad (2d)$$

where $d = \sqrt{w^2 + h^2}$, $\beta = \sin^{-1}(h/d)$ and $[x_0, y_0, \theta_0]$ denotes the initial position of m . From Eqns. (1a–d) and (2a–d), the elastic force vectors ($\vec{F}_{s,i}$) are then calculated with Hooke's law as:

$$F_{s,i} = -k_i \left(|\vec{r}_i - \vec{r}_{f,i}| - L_i \right) \frac{\vec{r}_i - \vec{r}_{f,i}}{|\vec{r}_i - \vec{r}_{f,i}|}. \quad i = 1, 2, 3, 4 \quad (3)$$

Finally, the governing equations of the system given in Fig. 1 are obtained as:

$$m\ddot{x} = F_{s,1x} + F_{s,2x} + \mu p_3(x, y, \theta) F_{s,3y} + \mu p_4(x, y, \theta) F_{s,4y}, \quad (4)$$

$$m\ddot{y} = F_{s,1y} + F_{s,2y} + p_3(x, y, \theta) F_{s,3y} + p_4(x, y, \theta) F_{s,4y} - F_n, \quad (5)$$

$$I\ddot{\theta} = -F_{s,1x}d \sin(\beta - \theta_0 - \theta) - F_{s,1y}d \cos(\beta - \theta_0 - \theta) - F_{s,2x}d \sin(\beta + \theta_0 + \theta) + F_{s,2y}d \cos(\beta + \theta_0 + \theta) - p_3(x, y, \theta) F_{s,3y}d \cos(\beta + \theta_0 + \theta) + \mu p_3(x, y, \theta) F_{s,3y}d \sin(\beta + \theta_0 + \theta) + p_4(x, y, \theta) F_{s,4y}d \cos(\beta - \theta_0 - \theta) + \mu p_4(x, y, \theta) F_{s,4y}d \sin(\beta - \theta_0 - \theta) \quad (6)$$

where $p_3(x, y, \theta)$ and $p_4(x, y, \theta)$ are defined as the Heaviside step function that is equal to 1 when m is in contact with the sliding surface but is 0 otherwise as expressed below:

$$p_i(x, y, \theta) = \begin{cases} 1 & |\vec{r}_i - \vec{r}_{f,i}| < L_i \\ 0 & |\vec{r}_i - \vec{r}_{f,i}| \geq L_i \end{cases}. \quad i = 3, 4 \quad (7)$$

Observe from Eqns. (4) to (6) that the restoring forces $F_{s,1}$ and $F_{s,2}$ have components in both \vec{e}_x and \vec{e}_y directions; however, the contact forces $F_{s,3}$ and $F_{s,4}$ have only

single components in the \vec{e}_y direction, although the contact forces also generate friction forces that are in \vec{e}_x direction. The governing equations (Eqns. (4)–(6)) of the three degree-of-freedom model of Fig. 1 exhibit clearance (due to the piecewise linear functions $p_i(x, y, \theta)$) and the kinematic nonlinearities (due to the $F_{s,ix}$ and $F_{s,iy}$ terms). Since $p_3(x, y, \theta)$ and $p_4(x, y, \theta)$ are discontinuous functions, Eqns. (4) to (6) may assume four different forms. The four states of the system of Fig. 1 are as follows: state 1, mass is in contact with the sliding surface at both leading and trailing edges ($F_{s,3} > 0$ and $F_{s,4} > 0$); state 2, surfaces of the contact interface are separated ($F_{s,3} = 0$ and $F_{s,4} = 0$); state 3, mass can secure contact only at the leading edge ($F_{s,3} > 0$ and $F_{s,4} = 0$); and state 4, contact occurs only at the trailing edge ($F_{s,3} = 0$ and $F_{s,4} > 0$). Observe that the system switches between these states according to the conditions listed in Table 1. Furthermore, the relationships between these states are depicted in Fig. 3. The numerical solutions of Eqns. (4) to (6) for different normal force vector arrangements are obtained by employing an event detection type algorithm²⁵, where the condition $|\vec{r}_i - \vec{r}_{f,i}| - L_i = 0$ is continuously tracked at both edges of m during the numerical integration. At the instance when this condition is detected at either edge, the governing equations are updated accordingly.

Table 1—Model B1 conditions used for the determination of states.

Condition Identifier	Expression	Slope
Condition 1-2	$ \vec{r}_3 - \vec{r}_{f,3} - L_3 = 0$	Positive
	$ \vec{r}_4 - \vec{r}_{f,4} - L_4 = 0$	Positive
Condition 2-1	$ \vec{r}_3 - \vec{r}_{f,3} - L_3 = 0$	Negative
	$ \vec{r}_4 - \vec{r}_{f,4} - L_4 = 0$	Negative
Condition 1-3	$ \vec{r}_4 - \vec{r}_{f,4} - L_4 = 0$	Positive
Condition 3-1	$ \vec{r}_4 - \vec{r}_{f,4} - L_4 = 0$	Negative
Condition 1-4	$ \vec{r}_3 - \vec{r}_{f,3} - L_3 = 0$	Positive
Condition 4-1	$ \vec{r}_3 - \vec{r}_{f,3} - L_3 = 0$	Negative
Condition 2-3	$ \vec{r}_3 - \vec{r}_{f,3} - L_3 = 0$	Negative
Condition 3-2	$ \vec{r}_3 - \vec{r}_{f,3} - L_3 = 0$	Positive
Condition 2-4	$ \vec{r}_4 - \vec{r}_{f,4} - L_4 = 0$	Negative
Condition 4-2	$ \vec{r}_4 - \vec{r}_{f,4} - L_4 = 0$	Positive

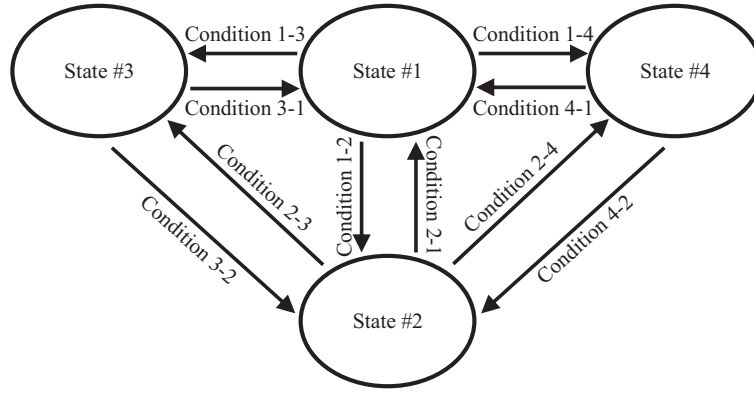


Fig. 3—State flow chart for model B1 and corresponding conditions (as in Table 1).

Equations (4) to (6) are numerically solved for the following four spring orientation angles α_1 and α_2 , which are selected arbitrarily: (a) $\alpha_1 = 0.5\pi$, $\alpha_2 = \pi$; (b) $\alpha_1 = \pi$, $\alpha_2 = 0.5\pi$; (c) $\alpha_1 = \alpha_2 = 0.75\pi$; and (d) $\alpha_1 = \alpha_2 = 0.83\pi$. The results are given in terms of normalized contact forces at leading ($\bar{F}_{s,3}$) and trailing ($\bar{F}_{s,4}$) edges, where the normalization is done by the actuation (brake) force F_n . Furthermore, the states observed in a particular configuration are depicted with a color code as follows: light blue (■) for state 1, black (■) for state 2, purple (■) for state 3, and red (■) for state 4. For the first case where $\alpha_1 = 0.5\pi$ and $\alpha_2 = \pi$, corresponding normalized contact forces are shown in Fig. 4. Here, consecutive impact-like forces are developed at both edges of the mass; i.e., contact forces at both edges go down to zero at certain time instances due to the surface separation. Furthermore, the amplitudes of the contact force at trailing edge (Fig. 4(b)) are higher than the amplitudes of the contact force at leading edge (Fig. 4(a)), and the dynamic responses include all four states of Fig. 3. In the second case where $\alpha_1 = \pi$ and $\alpha_2 = 0.5\pi$, contact loss occurs only at the trailing edge, but the contact is always maintained at the leading edge ($\bar{F}_{s,3} > 0$ for all t). Thus, only the state 1 and state 3 are observed. In addition, contact force amplitudes are almost three times higher at the leading edge (Fig. 5(a)) when compared to the amplitudes at the trailing edge (Fig. 5(b)). The next case ($\alpha_1 = \alpha_2 = 0.75\pi$) reveals an interesting situation (Fig. 6) where contact losses at both edges do not occur concurrently. Hence, at any instance, the mass is either in contact at both edges or in contact at one of the edges, i.e., $\bar{F}_{s,3} + \bar{F}_{s,4} > 0$ for all t . This implies that the impact-like forces again emerge at both edges. Therefore, all states except state 2 are observed for this particular configuration. For the last case ($\alpha_1 = \alpha_2 = 0.83\pi$), behavior similar to the previous case ($\alpha_1 = \alpha_2 = 0.75\pi$) is found. On the contrary, the mass remains at full contact with the sliding surface (state 1) for most of the event and instantaneous impact-like forces successively develop at the edges (Fig. 7).

5 LINE CONTACT (DISTRIBUTED STIFFNESS) FORMULATION (MODEL B2)

As shown in Fig. 2, the contact interface of model B2 is represented with the interfacial forces (R_n and R_f) between m and the sliding surface underneath. Observe that these forces are point forces and calculated through the integration of the distributed interfacial forces over the contact line. Furthermore, the forces R_n and R_f act on m from a distance of δ (in the \vec{e}_x direction) which changes with the motion of m .

Like the point contact formulation (model B1), the nonlinear governing equations of motion for this system are obtained again from the elastic force vectors (only $F_{s,1}$ and $F_{s,2}$). Similarly, these forces are again calculated by the Hooke's law (Eqn. (3)) with the help of the position vectors defined with Eqns. (1a, b) and (2a, b). Consequently, the governing equations for the model B2 are derived as follows:

$$m\ddot{x} = F_{s,1x} + F_{s,2x} + p(x, y, \theta)R_f, \quad (8)$$

$$m\ddot{y} = F_{s,1y} + F_{s,2y} + p(x, y, \theta)R_n - F_n, \quad (9)$$

$$I\ddot{\theta} = -F_{s,1x}d \sin(\beta - \theta_0 - \theta) - F_{s,1y}d \cos(\beta - \theta_0 - \theta) - F_{s,2x}d \sin(\beta + \theta_0 + \theta) + F_{s,2y}d \cos(\beta + \theta_0 + \theta) + p(x, y, \theta)hR_f + p(x, y, \theta)\delta R_n \quad (10)$$

where $p(x, y, \theta)$ is again the Heaviside step function as given by Eqn. (7). In order to solve these equations, it is necessary to calculate the interfacial normal force R_n and its action point δ , which depend on the instantaneous position of m (i.e., the leading $[x_t, y_t]$ or trailing $[x_t, y_t]$ edge of the contact region). The x coordinate of the contact loss point (x_{cl}) is calculated from the function of a line that passes through points $[x_l, y_l]$ and $[x_t, y_t]$, and crosses the

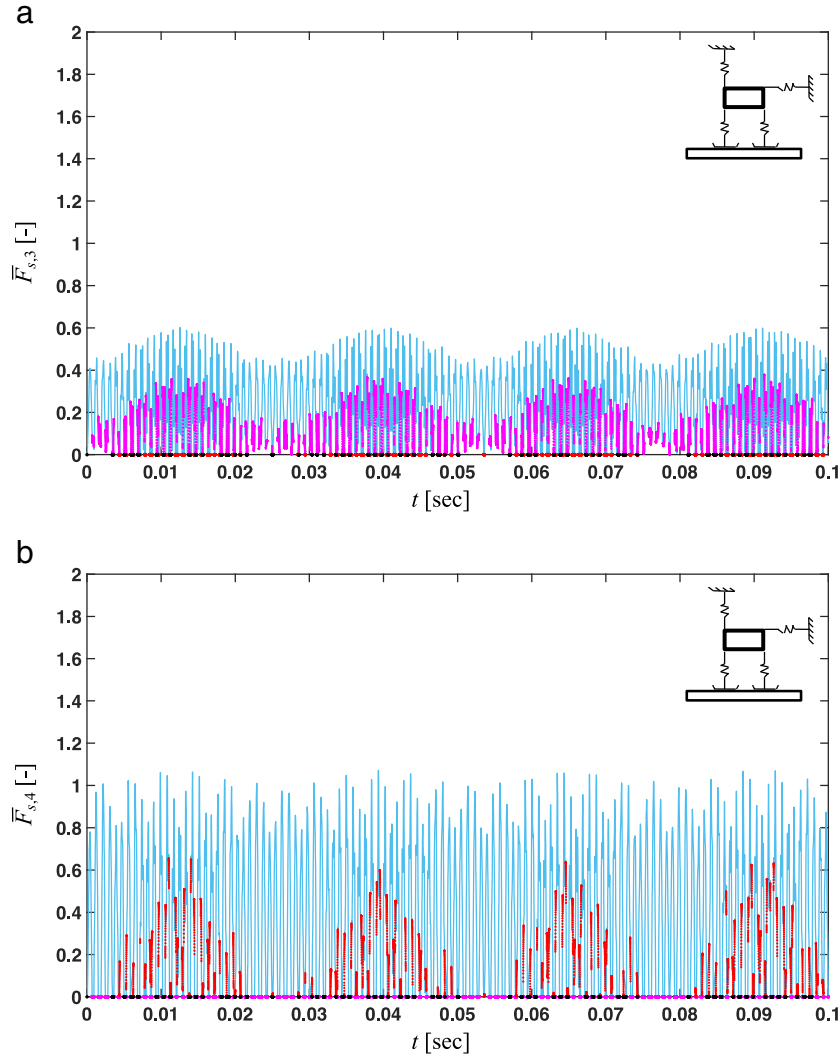


Fig. 4—Time histories of normalized contact forces for $\alpha_1 = 0.5\pi$, $\alpha_2 = \pi$ with model B1. (a) Leading edge contact force, $\bar{F}_{s,3} = F_{s,3}/F_n$; (b) Trailing edge contact force, $\bar{F}_{s,4} = F_{s,4}/F_n$. Observe that all states of Fig. 3 are observed. Key: —, state 1; —, state 2; —, state 3; —, state 4.

point $y_{cl} = -h$. The coordinates of the leading and trailing edges are defined as:

$$x_l = x_0 + x - d \cos(\beta + \theta_0 + \theta), \quad (11a)$$

$$y_l = y_0 + y - d \sin(\beta + \theta_0 + \theta), \quad (11b)$$

$$x_t = x_0 + x + d \cos(\beta - \theta_0 - \theta), \quad (11c)$$

$$y_t = y_0 + y - d \sin(\beta - \theta_0 - \theta). \quad (11d)$$

The coordinate $[x_{cl}, y_{cl}]$ is the contact loss point where the expression for x_{cl} is:

$$x_{cl} = x_0 + x - (y_0 + y + h) \cot(\theta_0 + \theta) + d \frac{\sin(\beta)}{\sin(\theta_0 + \theta)}. \quad (12)$$

Note that Eqn. (12) is not defined for $\theta_0 + \theta = 0$. When this condition is satisfied, m stays parallel to the sliding surface. Thus, the reaction force R_n should act on m at its center ($\delta = 0$). Two cases can emerge that denote the surface separation and full contact. Further, an additional partial contact case can also occur when $\theta_0 + \theta \neq 0$. All of these cases are summarized in Table 2 along with their conditions. Note that x_{cl} alone cannot be used to determine the state of m when $\theta_0 + \theta = 0$ since Eqn. (12) is not defined.

The normal reaction force R_n for all cases of Table 2 can be calculated as the integral of the distributed force at the contact line. Note that $R_n \geq 0$ at any t since it represents the interfacial contact force. Based on the value of x_{cl} as given in Table 2, the value of R_n should be:

$$R_n = \frac{1}{x_U - x_L} \int_{x_L}^{x_U} \left(k_c(y_l - y_{cl}) + k_c(s - x_l) \frac{y_t - y_l}{x_t - x_l} \right) ds, \quad (13)$$

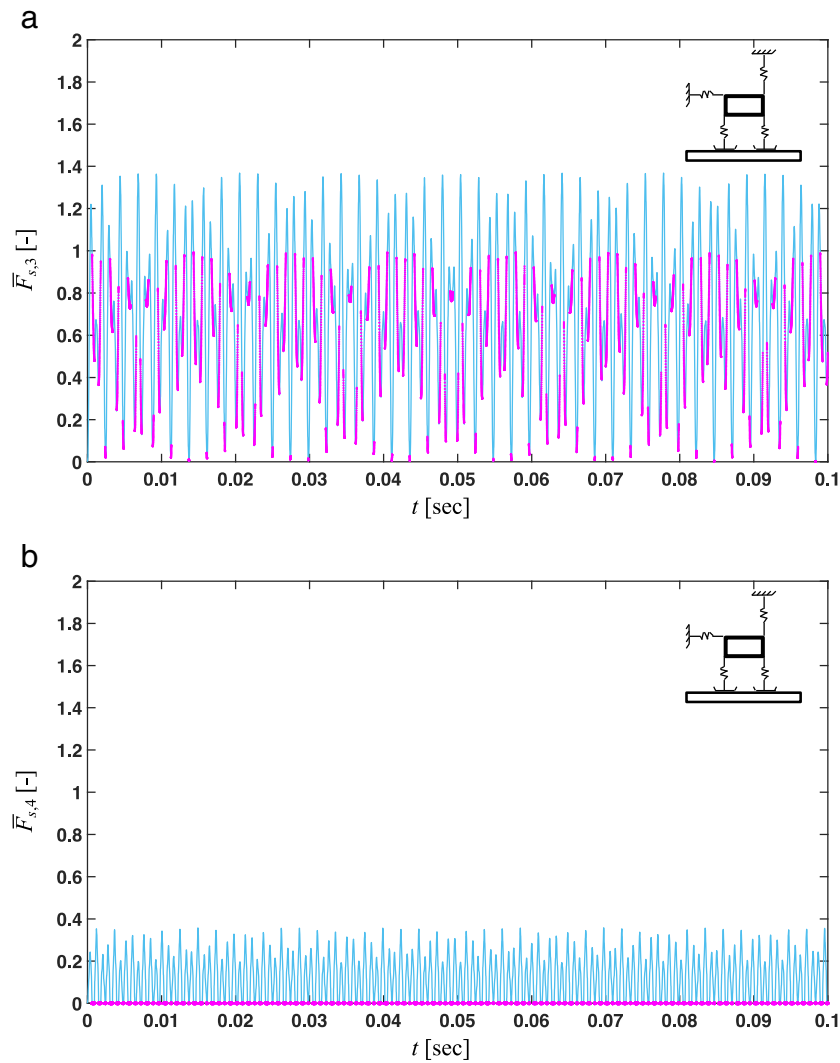


Fig. 5—Time histories of normalized contact forces for $\alpha_1 = \pi$, $\alpha_2 = 0.5\pi$ with model B1. (a) Leading edge contact force, $\bar{F}_{s,3} = F_{s,3}/F_n$; (b) Trailing edge contact force, $\bar{F}_{s,4} = F_{s,4}/F_n$. Observe that only states 1 and 3 are observed. Key: —, state 1; —, state 3.

where k_c is the contact stiffness per unit length, and x_L and x_U are the lower and upper limits of the integral that represent leading and trailing edges of the contact line, respectively. For example, $(x_L, x_U) = (x_l, x_t)$ for the full contact cases. However, $(x_L, x_U) = (x_l, x_{cl})$ or $(x_L, x_U) = (x_{cl}, x_t)$ for the partial contact cases based on the sign of $(\theta_0 + \theta)$. This implies that $(x_L, x_U) = (x_l, x_{cl})$ for $\theta_0 + \theta > 0$ and $(x_L, x_U) = (x_{cl}, x_t)$ for $\theta_0 + \theta < 0$. Assigning the proper integral limits in Eqn. (13), R_n is determined below for all cases of Table 2.

a. For $\theta_0 + \theta > 0$:

$$R_n = 0, \quad x_{cl} \leq x_l \quad (14a)$$

$$R_n = -0.5k_c(y_0 + y + h - d \sin(\beta + \theta_0 + \theta)), \quad x_l < x_{cl} < x_t \quad (14b)$$

$$R_n = -k_c(y_0 + y + h - d \sin(\beta) \cos(\theta_0 + \theta)), \quad x_{cl} \geq x_t \quad (14c)$$

b. For $\theta_0 + \theta = 0$:

$$R_n = -k_c(y_0 + y + h - d \sin(\beta)), \quad y + y_0 < 0 \quad (15a)$$

$$R_n = 0, \quad y + y_0 \geq 0 \quad (15b)$$

c. For $\theta_0 + \theta < 0$:

$$R_n = -k_c(y_0 + y + h - d \sin(\beta) \cos(\theta_0 + \theta)), \quad x_{cl} \leq x_l \quad (16a)$$

$$R_n = -0.5k_c(y_0 + y + h - d \sin(\beta - \theta_0 - \theta)), \quad x_l < x_{cl} < x_t \quad (16b)$$

$$R_n = 0, \quad x_{cl} \geq x_t \quad (16c)$$

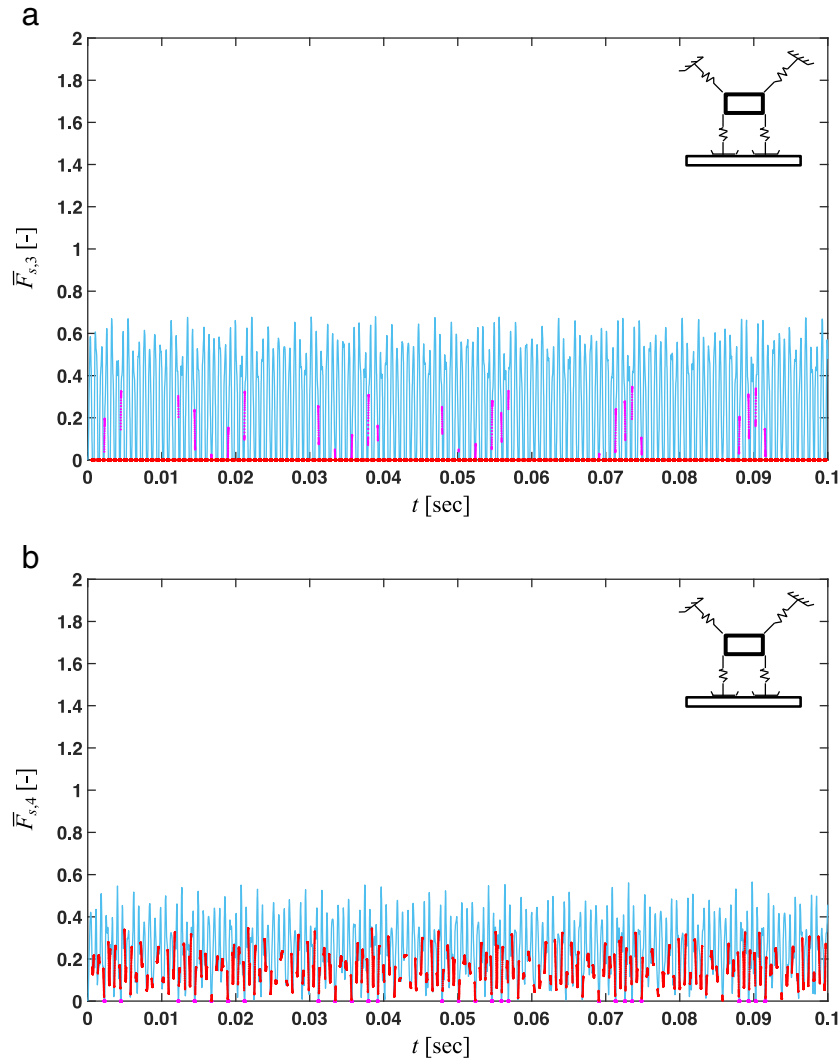


Fig. 6—Time histories of normalized contact forces for $\alpha_1 = \alpha_2 = 0.75\pi$ with model B1. (a) Leading edge contact force, $\bar{F}_{s,3} = F_{s,3}/F_n$; (b) Trailing edge contact force, $\bar{F}_{s,4} = F_{s,4}/F_n$. Observe that states 1, 3 and 4 are observed. Key: —, state 1; —, state 3; —, state 4.

Similarly, the point where R_n acts on m (as defined with δ on Fig. 2) is calculated with the following equation:

$$\delta = \frac{\int_{x_L}^{x_U} \left(k_c s (y_l - y_{cl}) + k_c s (s - x_l) \frac{y_l - y_l}{x_l - x_l} \right) ds}{\int_{x_L}^{x_U} \left(k_c (y_l - y_{cl}) + k_c (s - x_l) \frac{y_l - y_l}{x_l - x_l} \right) ds}, \quad (17)$$

where the limits of the integral are the same as for Eqn. (13). Overall, the action points δ of the interfacial reaction force R_n for all cases of Table 2 are obtained as below:

a. For $\theta_0 + \theta > 0$:

$$\delta : \text{Does not exist, } x_{cl} \leq x_l \quad (18a)$$

$$\delta = \frac{2x_l + x_{cl}}{3}, \quad x_l < x_{cl} < x_t \quad (18b)$$

$$\delta = \frac{2x_l y_l - 3x_t y_{cl} - 3x_l y_{cl} + x_l y_t + x_t y_l + 2x_t y_t}{3(y_l + y_t - 2y_{cl})}, \quad x_{cl} \geq x_t \quad (18c)$$

b. For $\theta_0 + \theta = 0$:

$$\delta = 0, \quad y + y_0 < 0 \quad (19a)$$

$$\delta : \text{Does not exist, } y + y_0 \geq 0 \quad (19b)$$

c. For $\theta_0 + \theta < 0$:

$$\delta = \frac{2x_l y_l - 3x_t y_{cl} - 3x_l y_{cl} + x_l y_t + x_t y_l + 2x_t y_t}{3(y_l + y_t - 2y_{cl})}, \quad x_{cl} \leq x_l \quad (20a)$$

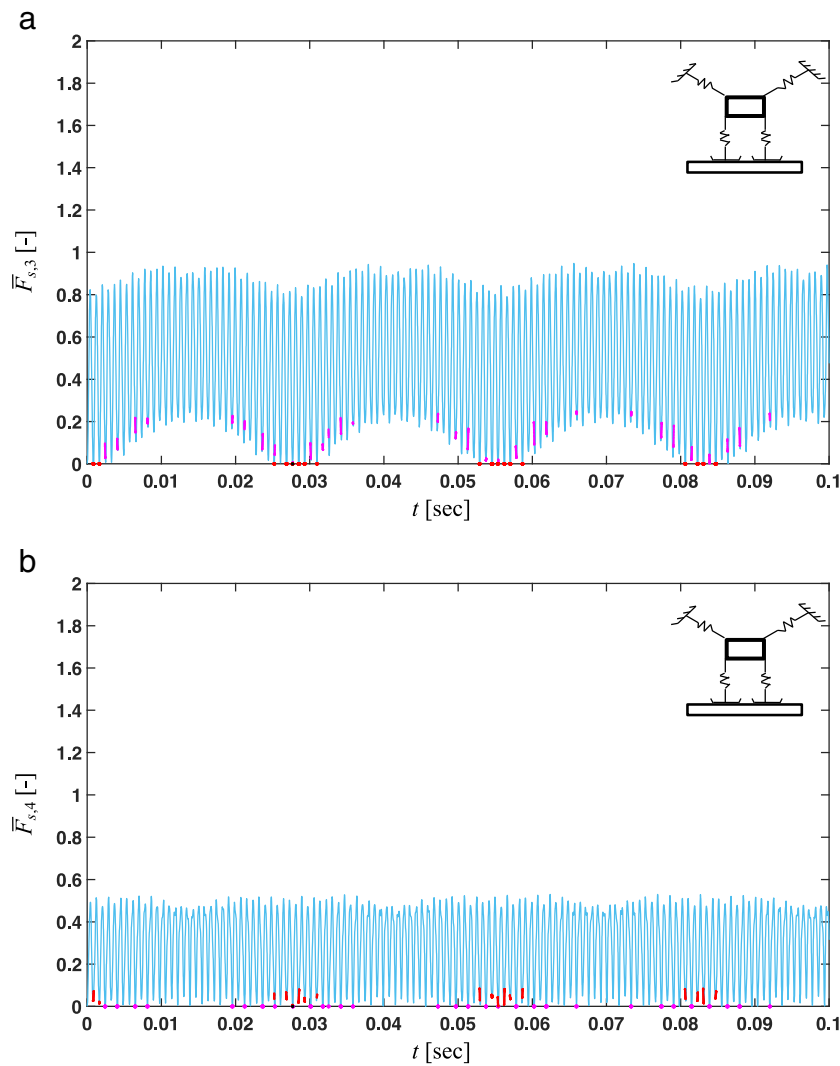


Fig. 7—Time histories of normalized contact forces for $\alpha_1 = \alpha_2 = 0.83\pi$ with model B1. (a) Leading edge contact force, $\bar{F}_{s,3} = F_{s,3}/F_n$; (b) Trailing edge contact force, $\bar{F}_{s,4} = F_{s,4}/F_n$. Observe that states 1, 3 and 4 are observed. Key: —, state 1; —, state 2; —, state 3; —, state 4.

$$\delta = \frac{2x_t + x_{cl}}{3}, \quad x_l < x_{cl} < x_t \quad (20b)$$

$$\delta : \text{Does not exist.} \quad x_{cl} \geq x_t \quad (20c)$$

Observe that δ does not exist when $R_n = 0$ since the surfaces are separated.

The governing equations of model B2 (Eqns. (8)–(10)) are piecewise nonlinear. This implies that the dynamics may be represented with different sets of nonlinear equations based on the states of Table 2. These equations are numerically solved by tracking the given conditions and updating the governing equations when an event is detected like in model B1. The state flow chart for model B2 is shown in Fig. 8. Like the model with point contacts at edges, results are again obtained for the same geometric arrangements of the angles α_1 and α_2 . Typical results

are given in terms of R_n and δ (when normalized with respect to F_n and w , respectively) in Figs. 9 to 12. Observe in Fig. 9 (for $\alpha_1 = 0.5\pi$ and $\alpha_2 = \pi$) that the mass always maintains contact with the sliding surface since $\bar{R}_n > 0$ at all times. Furthermore, $\bar{\delta} < 0$ at any t ; this means the position of the reaction force \bar{R}_n is in between the center and the leading edge, i.e., $\theta_0 + \theta > 0$ at any t . Similarly, the mass remains in contact with the sliding surface for the case where $\alpha_1 = \pi$ and $\alpha_2 = 0.5\pi$ (Fig. 10). However, the position of \bar{R}_n varies in between the center of mass and trailing edge when $\bar{\delta} > 0$, i.e. $\theta_0 + \theta < 0$ for all t . Furthermore, the calculated \bar{R}_n in this case is almost twice of \bar{R}_n of the previous case where $\alpha_1 = 0.5\pi$ and $\alpha_2 = \pi$ (Fig. 9(a)). This is explained by the angular arrangements of the springs (α_1 and α_2) and the direction of sliding surface velocity. Observe that the friction force (in between the mass and its sliding surface) tends to increase the

Table 2—Model B2 conditions for the status of contact between the mass and sliding surface.

	$x_{cl} \leq x_l$	Surface separation
$\theta_0 + \theta > 0$	$x_l < x_{cl} < x_t$	Partial contact
	$x_{cl} \geq x_t$	Full contact
$\theta_0 + \theta = 0$	$y + y_0 < 0$	Full contact
	$y + y_0 \geq 0$	Surface separation
$\theta_0 + \theta < 0$	$x_{cl} \leq x_l$	Full contact
	$x_l < x_{cl} < x_t$	Partial contact
	$x_{cl} \geq x_t$	Surface separation

reaction force in the second case; this is a mechanism for the sprag-slip behavior, although this type of response is not observed in the solutions. The results for $\alpha_1 = \alpha_2 = 0.75\pi$ (in Fig. 11) exhibit a different dynamic behavior. For instance, the mass loses contact with the sliding surface (in Fig. 11(a)) when $\bar{R}_n = 0$. Furthermore, the reaction force location $\bar{\delta}$ successively moves toward the leading and trailing edges thereby mimicking the hammering behavior. The last case ($\alpha_1 = \alpha_2 = 0.83\pi$) as shown in Fig. 12 is yet another perpetual contact case between the mass and the sliding surface, and now the location of reaction force $\bar{\delta}$ is always in between the center of the mass and its trailing edge.

From the hammering behavior perspective, it is seen that model B1 exhibits surface separation for all angular configurations being investigated. Therefore, one can argue that the hammering phenomenon is observed for any configuration with model B1 due to the impact-like forces that emerge at the contact interface though there are significant differences as explained before. However, the surface separation is observed only with the $\alpha_1 = \alpha_2 = 0.75\pi$ configuration with model B2. The surfaces remain in contact for the other configurations, although the mass represents

an angular displacement. However, this angular motion does not seem to generate impact-like forces. Thus, the hammering dynamics is observed only with the $\alpha_1 = \alpha_2 = 0.75\pi$ angular configuration with model B2. Therefore, it is concluded that model B1 exaggerates the dynamic responses by representing the contact loss behavior for all cases. In addition, responses of both models support each other from certain perspectives as well. For example, the configuration of mass in both models can be represented as $\theta_0 + \theta > 0$ at any t in the second case ($\alpha_1 = \pi$ and $\alpha_2 = 0.5\pi$) leading to contact losses only at the vicinity of the trailing edge. Furthermore, the third case ($\alpha_1 = \alpha_2 = 0.75\pi$) is evidently the only one where hammering phenomenon is severely observed with both models.

6 EXISTENCE OF QUASI-STATIC SLIDING MOTION (MODEL B3)

In order to obtain the angular configurations where hammering phenomenon could be observed, the existence of quasi-static sliding behavior must be investigated. Note that this represents a motion state with zero acceleration along with a perpetual contact at the disc/pad interface; i.e., it contradicts the hammering behavior premise. Accordingly, model B2 is simplified with some assumptions. First, the Heaviside step function is dropped from the governing equations (Eqns. (8)–(10)); i.e., $p(x, y, \theta) = 1$ is assumed. Second, Eqns. (8) to (10) are linearized around the origin $[x, y, \theta] = [0, 0, 0]$. Thus, Eqns. (8) to (10) are written in the matrix form as follows:

$$\begin{bmatrix} m & 0 & 0 \\ 0 & m & 0 \\ 0 & 0 & I \end{bmatrix} \begin{Bmatrix} \ddot{x} \\ \ddot{y} \\ \ddot{\theta} \end{Bmatrix} + \begin{bmatrix} K_{11} & K_{12} & K_{13} \\ K_{21} & K_{22} & K_{23} \\ K_{31} & K_{32} & K_{33} \end{bmatrix} \begin{Bmatrix} x \\ y \\ \theta \end{Bmatrix} = \begin{Bmatrix} R_f \\ R_n - F_n \\ R_f h - R_n \delta \end{Bmatrix}, \quad (21)$$

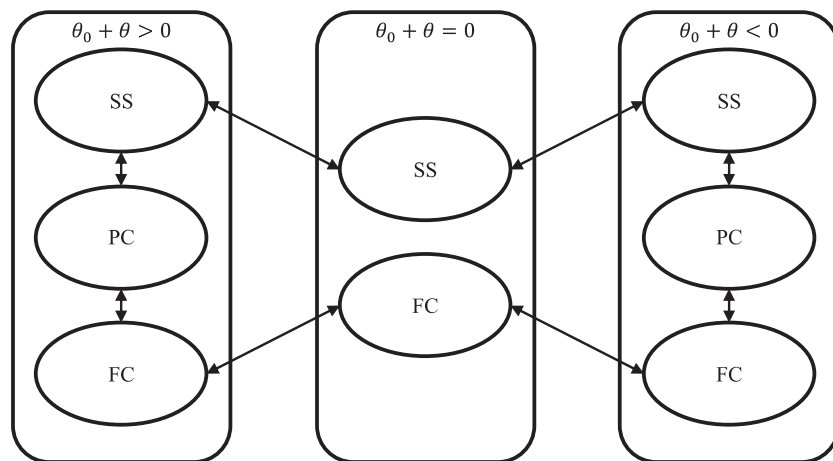


Fig. 8—State flow chart for model B2 where the abbreviations are as follows: SS, surface separation; PC, partial contact; and FC, full contact.

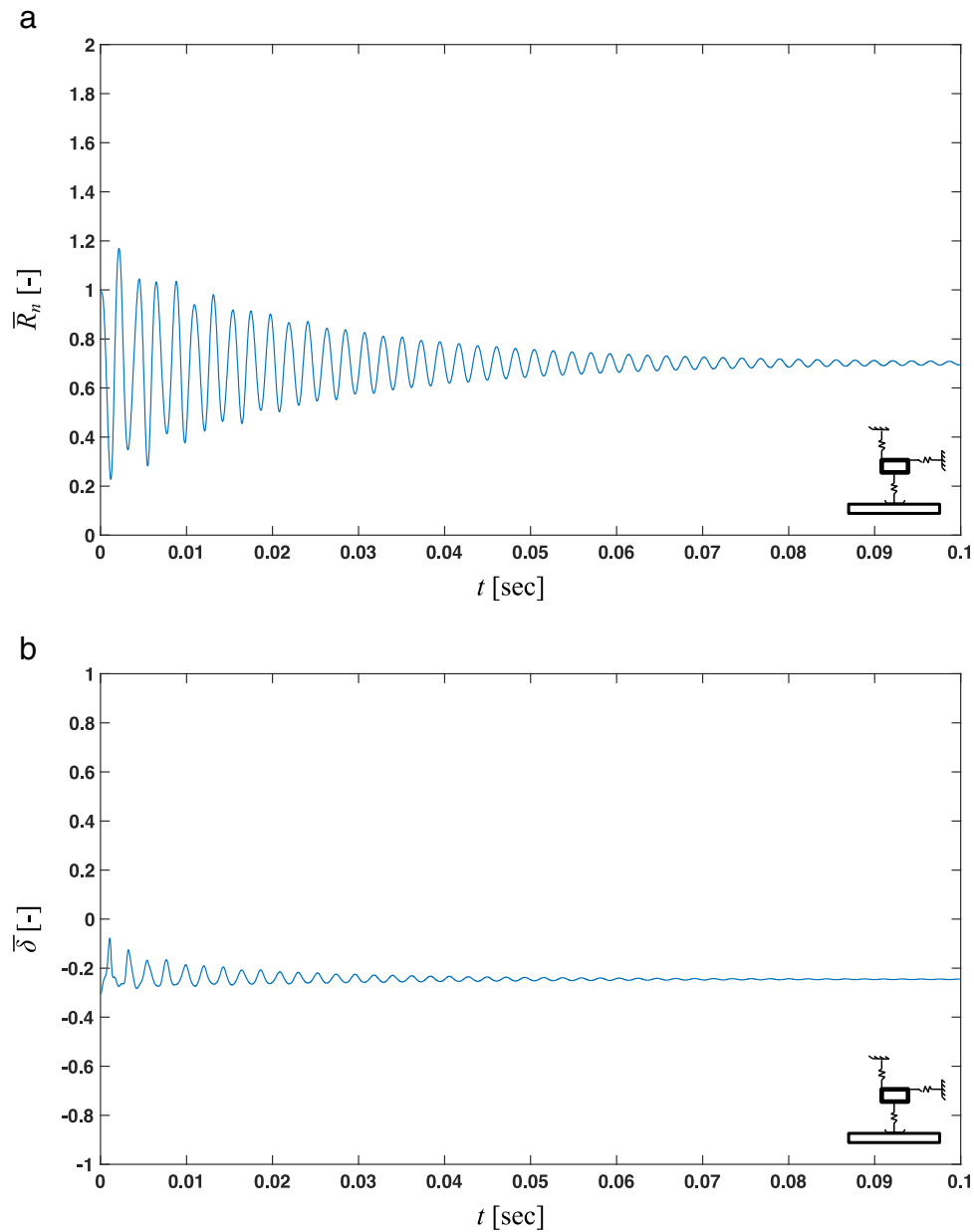


Fig. 9—Time histories of normalized reaction force magnitude and position using model B2 for $\alpha_1 = 0.5\pi, \alpha_2 = \pi$. (a) Normalized reaction force, $\bar{R}_n = R_n/F_n$; (b) Normalized position of the reaction force, $\bar{\delta} = \delta/w$.

where:

$$K_{11} = k_1 \cos^2(\alpha_1) + k_2 \cos^2(\alpha_2), \quad (22a)$$

$$K_{12} = k_1 \sin(\alpha_1) \cos(\alpha_1) - k_2 \sin(\alpha_2) \cos(\alpha_2), \quad (22b)$$

$$K_{13} = -dk_1 \cos(\alpha_1) \sin(\alpha_1 + \beta - \theta_0) - dk_2 \cos(\alpha_2) \sin(\alpha_2 + \beta + \theta_0), \quad (22c)$$

$$K_{21} = k_1 \sin(\alpha_1) \cos(\alpha_1) - k_2 \sin(\alpha_2) \cos(\alpha_2), \quad (22d)$$

$$K_{22} = k_1 \sin^2(\alpha_1) + k_2 \sin^2(\alpha_2), \quad (22e)$$

$$K_{23} = -dk_1 \sin(\alpha_1) \sin(\alpha_1 + \beta - \theta_0) + dk_2 \sin(\alpha_2) \sin(\alpha_2 + \beta + \theta_0), \quad (22f)$$

$$K_{31} = -dk_1 \cos(\alpha_1) \sin(\alpha_1 + \beta - \theta_0) - dk_2 \cos(\alpha_2) \sin(\alpha_2 + \beta + \theta_0), \quad (22g)$$

$$K_{32} = -dk_1 \sin(\alpha_1) \sin(\alpha_1 + \beta - \theta_0) + dk_2 \sin(\alpha_2) \sin(\alpha_2 + \beta + \theta_0), \quad (22h)$$

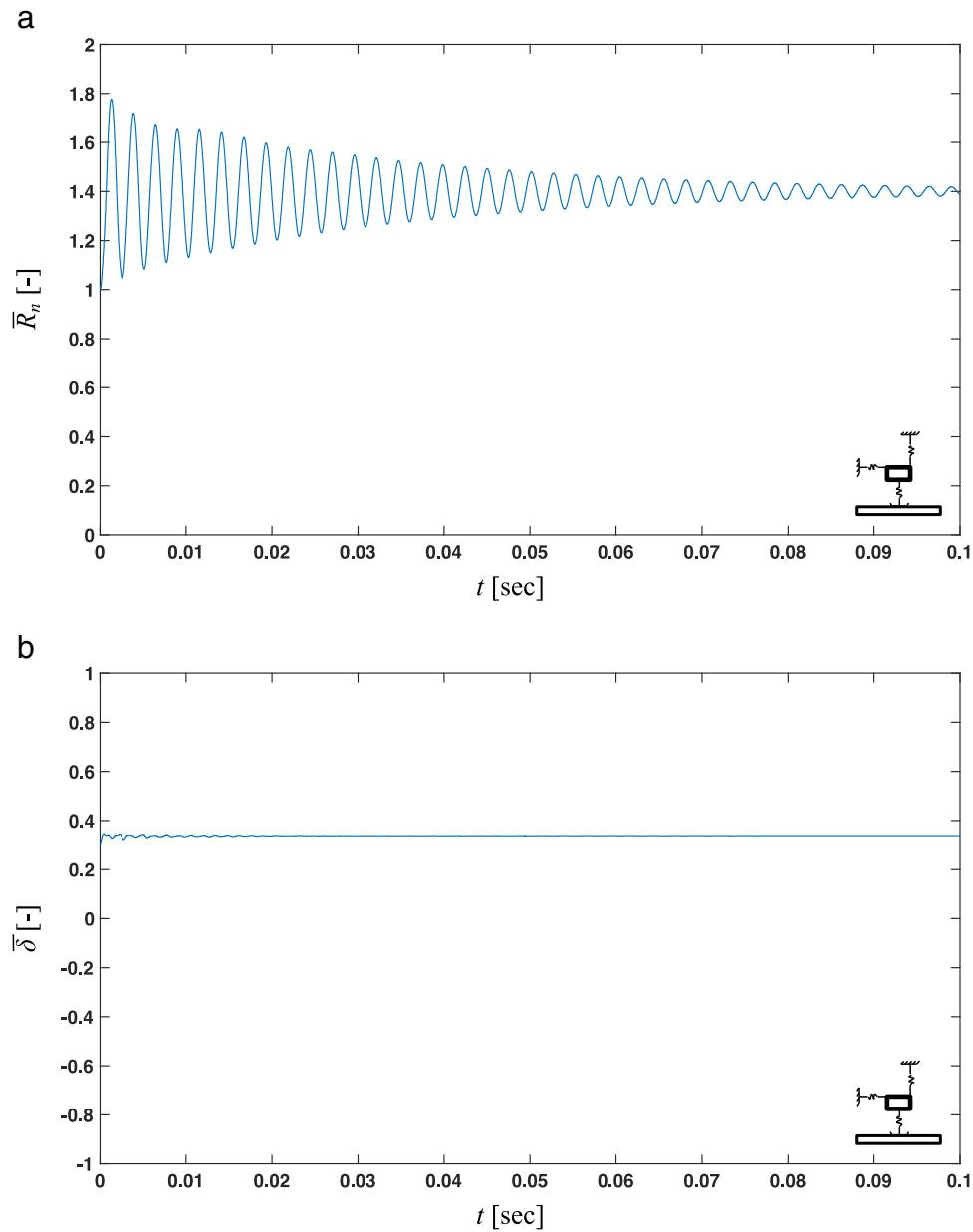


Fig. 10—Time histories of normalized reaction force magnitude and position using model B2 for $\alpha_1 = \pi$, $\alpha_2 = 0.5\pi$. (a) Normalized reaction force, $\bar{R}_n = R_n/F_n$; (b) Normalized position of the reaction force, $\bar{\delta} = \delta/w$.

$$K_{33} = d^2 k_1 \sin(\alpha_1 + \beta - \theta_0) (\sin(\beta - \theta_0) \cos(\alpha_1) + \cos(\beta - \theta_0) \sin(\alpha_1)) \quad (22i)$$

The quasi-static sliding motion is sought for $\dot{x} = 0$, $\dot{y} = 0$ and $\dot{\theta} = 0$. The system of linear differential equations (Eqn. (21)) now reduces to a set of non-homogeneous algebraic equations with a coefficients matrix whose elements are given by Eqns. (22a–i). Further investigation of the coefficients matrix reveals that it is a singular matrix. This implies that either the solution does not exist or it is not unique. Therefore, the existence of the quasi-static sliding

motion is only checked for the $y = 0$ and $\theta = 0$ case which corresponds to m essentially sitting on the sliding surface with zero angular displacement, and thus, $\delta = 0$. Hence, m is in a line contact with the sliding surface, i.e., all the way from the leading to trailing edge. Consequently, the following conditions are obtained for the existence of the quasi-static sliding motion:

$$\mu < \frac{K_{11}}{K_{21}}, \quad (23a)$$

$$\mu < \frac{K_{31}}{hK_{21}}. \quad (23b)$$

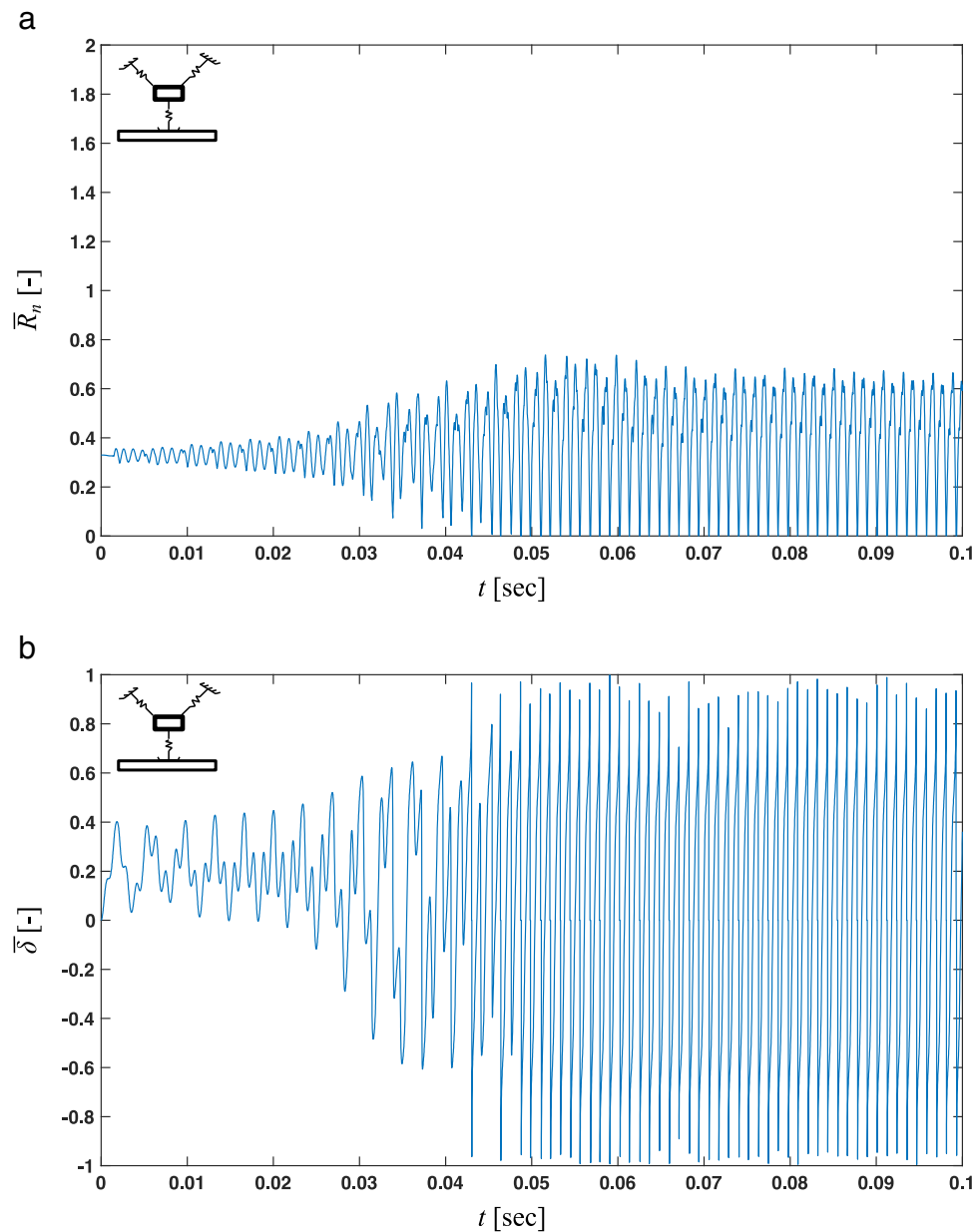


Fig. 11—Time histories of normalized reaction force magnitude and position using model B2 for $\alpha_1 = \alpha_2 = 0.75\pi$. (a) Normalized reaction force, $R_n = R_n/F_n$; (b) Normalized position of the reaction force, $\bar{\delta} = \delta/w$.

Observe that Eqns. (23a) and (23b) are obtained with the Coulomb friction assumption, i.e., $R_f = \mu R_n$. These conditions are checked for $0 < \alpha_1 < \pi$ and $0 < \alpha_2 < \pi$, and the corresponding map is illustrated in Fig. 13. The quasi-static sliding motion is only possible in the black region of the map. Here the numerical solutions of model B2 reveal perpetual contact behavior ($p(x, y, \theta) = 1$ at any t) for some cases, which is one of the assumptions made while obtaining model B3. However, there is a clear distinction between quasi-static sliding behavior and perpetual contact case since the acceleration of the mass is zero in the former one. Further investigation of those cases show that the acceleration of the mass is not zero; hence, the quasi-static sliding behavior cannot be assumed.

7 CONCLUSION

The chief contribution of this article is the development of a refined three degree-of-freedom brake system model with two different contact stiffness formulations, where model B1 assumes point contacts only at leading and trailing edges of the mass and model B2 proposes a line contact over the entire interface. The nonlinear governing equations of both models are numerically solved for selected angular configurations of the inclined springs. Overall, the hammering behavior is successfully observed in one particular angular configuration with both contact formulations. Nevertheless, model B1 has certain limitations; i.e., perpetual contact cases could not be obtained.

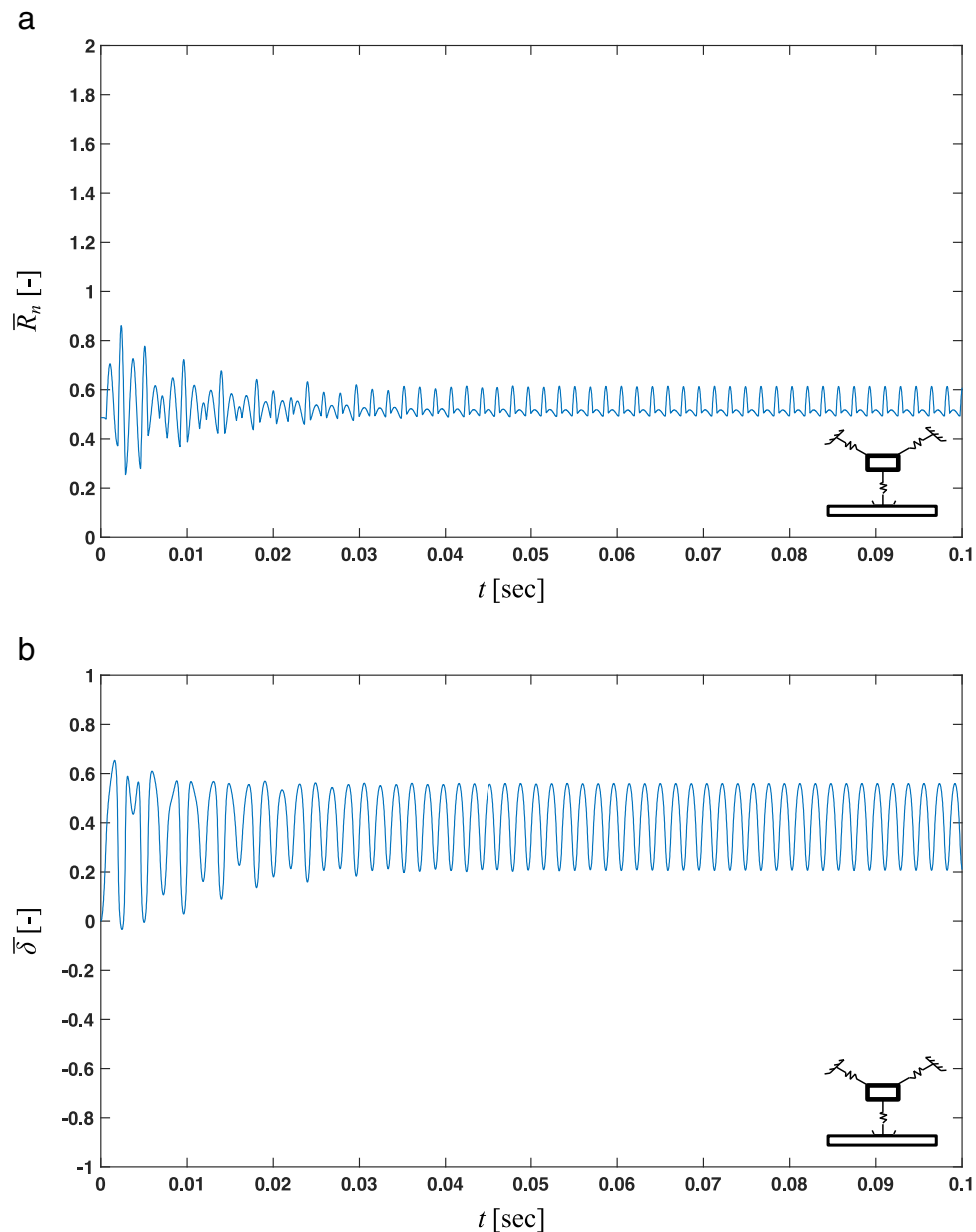


Fig. 12—Time histories of normalized reaction force magnitude and position using model B2 for $\alpha_1 = \alpha_2 = 0.83\pi$. (a) Normalized reaction force, $\bar{R}_n = R_n/F_n$; (b) Normalized position of the reaction force, $\bar{\delta} = \delta/w$.

The quasi-static sliding motion is then investigated with model B3 with certain assumptions. The investigation suggests that the quasi-static sliding motion is only possible over a small region of $\alpha_1 = [0, \pi]$ and $\alpha_2 = [0, \pi]$ map. Furthermore, quasi-static sliding behavior has not been observed on any of the cases analyzed with models B1 and B2.

Refined models of this article reveal the essential nature of the hammering behavior which is one of the source mechanisms of brake squeal. The hammering phenomenon has been experimentally observed by several researchers; thus, the findings of the current article are qualitatively supported. In particular, Butlin and Woodhouse²⁶ and Meziane et al.²⁷ successfully observed detachment of the mating surfaces in

their laboratory experiments where the noise emitted is related to the impact forces caused by the successive contact and detachment regimes. Nevertheless, their chief observation was that the interface contact formulation has an important effect on the dynamic behavior and models with only discrete contacts lead to misinterpretations. This observation is consistent with the work of Oura et al.¹⁹, who claimed that the results of the model with distributed contact stiffness matches well with their measurements. However, Oura et al.¹⁹ did not investigate the effect of system kinematic configuration; the results of the current article suggest that the contact stiffness issue is a key factor for squeal noise initiation. Furthermore, the rotational degree

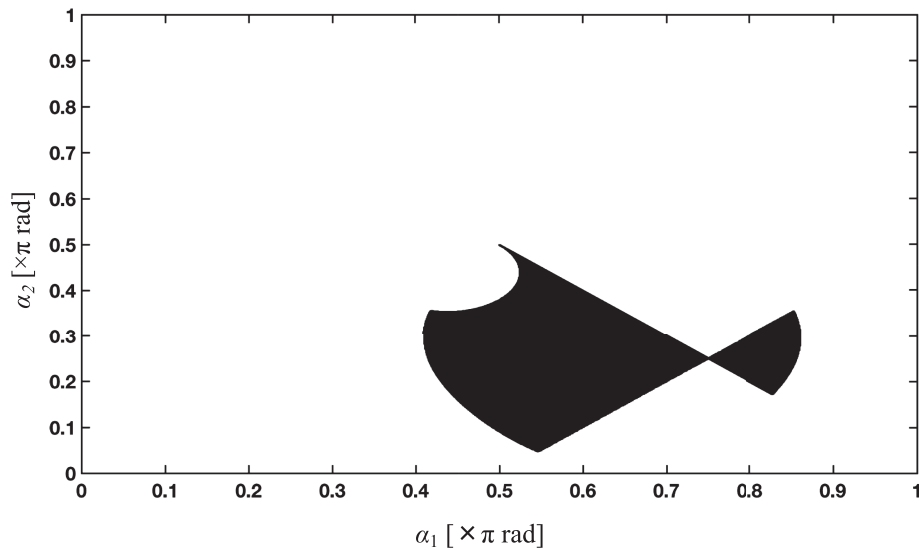


Fig. 13—Map of the quasi-static sliding motion for the linearized three degree-of-freedom model (model B3). Quasi-static sliding is only possible in the black shaded regions.

of freedom that was previously ignored in a two degree-of-freedom model by Sen et al.²⁰ is found to be important for the initiation of hammering behavior. The current article provides a clear understanding of the role of normal force vector directions in influencing the initiation of hammering behavior. This issue is promising from the noise control perspective as the brake pad design itself might be used to suppress the squeal noise; this aspect has not been addressed in the prior literature. Finally, a bench type brake-pad experiment is needed in future to validate the clues reported in this article to fully explore the hammering type squeal phenomena.

8 ACKNOWLEDGMENTS

Support from the Scientific and Technological Research Council of Turkey (3001 Starting R&D Projects Funding Program, Project No. 115 M002) and Scientific Research Projects Coordination Unit at Istanbul Technical University (Project No. MGA-2018-41304) is gratefully acknowledged by the first author. The second author thanks the National Science Foundation's IUCRC program (www.nsf.gov/eng/iip/iucrc) and the Smart Vehicle Concepts Center (www.SmartVehicleCenter.org) for partially supporting this research.

9 REFERENCES

1. N.M. Kinkaid, O.M. O'Reilly, and P. Papadopoulos, "Automotive disc brake squeal", *J. Sound Vib.*, **267**(1), 105–166, (2003).
2. A. Papinniemi, J.C.S. Lai, J. Zhao, and L. Loader, "Brake squeal: a literature review", *Appl. Acoust.*, **63**(4), 391–400, (2002).
3. H. Hetzler and K. Willner, "On the influence of contact tribology on brake squeal", *Tribol. Int.*, **46**(1), 237–246, (2012).
4. Y. Yue and L. Zhang, "A study of effects of brake contact interfaces on brake squeal", *SAE Int. J. Passeng. Cars – Mech. Syst.*, **2**(1), 1406–1413, (2009).
5. M. Eriksson, F. Bergman, and S. Jacobson, "On the nature of tribological contact in automotive brakes", *Wear*, **252**(1–2), 26–36, (2002).
6. P. Ioannidis, P.C. Brooks, and D.C. Barton, Drum Brake Contact Analysis and its Influence on Squeal Noise Prediction, In *21st Annual Brake Colloquium & Exhibition*. SAE International, (2002). <https://doi.org/10.4271/2003-01-3348>.
7. T. Hamabe, I. Yamazaki, K. Yamada, H. Matsui, S. Nakagawa, and M. Kawamura, Study of a Method for Reducing Drum Brake Squeal. In *International Congress & Exposition*. SAE International, (1999). <https://doi.org/10.4271/1999-01-0144>.
8. N. Hoffmann, M. Fischer, R. Allgaier, and L. Gaul, "A minimal model for studying properties of the mode-coupling type instability in friction induced oscillations", *Mech. Res. Commun.*, **29**, 197–205, (2002).
9. U.V. Wagner, D. Hochlenert, and P. Hagedorn, "Minimal models for disk brake squeal", *J. Sound Vib.*, **302**, 527–539, (2007).
10. A. Nobari, H. Ouyang, and P. Bannister, "Statistics of complex eigenvalues in friction-induced vibration", *J. Sound Vib.*, **338**, 169–183, (2015).
11. M. Stender, M. Tiedemann, N. Hoffmann, and S. Oberst, "Impact of an irregular friction formulation on dynamics of a minimal model for brake squeal", *Mech. Syst. Signal Pr.*, **107**, 439–451, (2018).
12. K. Soobbarayan, S. Besset, and J.-J. Sinou, "Noise and vibration for a self-excited mechanical system with friction", *Appl. Acoust.*, **74**(10), 1191–1204, (2013).
13. S. Oberst, J.C.S. Lai, and S. Marburg, "Guidelines for numerical vibration and acoustic analysis of disc brake squeal using simple models of brake systems", *J. Sound Vib.*, **332**(9), 2284–2299, (2013).
14. S. Oberst and J.C.S. Lai, "Pad-mode-induced instantaneous mode instability for simple models of brake systems", *Mech. Syst. Signal Pr.*, **62–63**, 490–505, (2015).
15. P. Liu, H. Zheng, C. Cai, Y.Y. Wang, C. Lu, K.H. Ang, and G.R. Liu, "Analysis of disc brake squeal using the complex eigenvalue method", *Appl. Acoust.*, **68**(6), 603–615, (2007).
16. F. Massi, L. Baillet, O. Giannini, and A. Sestieri, "Brake squeal: linear and nonlinear numerical approaches", *Mech. Syst. Signal Pr.*, **21**(6), 2374–2393, (2007).
17. F. Renaud, G. Chevallier, J.-L. Dion, and G. Taudiere, "Motion capture of a pad measured with accelerometers during squeal noise in a real brake system", *Mech. Syst. Signal Pr.*, **33**, 155–166, (2012).

18. A. Elmaian, F. Gautier, C. Pezerat, and J.-M. Duffal, "How can automotive friction-induced noises be related to physical mechanisms?" *Appl. Acoust.*, **76**, 391–401, (2014).
19. Y. Oura, Y. Kurita, Y. Matsumura, and Y. Nishizawa, Influence of Distributed Stiffness in Contact Surface on Disk Brake Squeal. In *26th Brake Colloquium and Exhibition*. SAE International, (2008). <https://doi.org/10.4271/2008-01-2584>.
20. O.T. Sen, J.T. Dreyer, and R. Singh, "An improved brake squeal source model in the presence of kinematic and friction nonlinearities", *INTER-NOISE 2013 Proceedings*, **247**(8), 438–446, (2013).
21. N.M. Ghazaly, M. El-Sharkawy, and I. Ahmed, "A review of automotive brake squeal mechanisms", *J. Mech. Des. Vib.*, **1**(1), 5–9, (2014).
22. R.T. Spurr, "A theory of brake squeal", *Proc. Inst. Mech. Eng., Part D*, **1**, 33–52, (1961).
23. J.-J. Sinou, F. Thouverez, and L. Jezequel, "Analysis of friction and instability by the centre manifold theory for a non-linear sprag-slip model", *J. Sound Vib.*, **265**, 527–559, (2003).
24. N. Hoffmann and L. Gaul, "A sufficient criterion for the onset of sprag-slip oscillations", *Arch. Appl. Mech.*, **73**, 650–660, (2004).
25. O.T. Sen, J.T. Dreyer, and R. Singh, "Order domain analysis of speed-dependent friction induced torque in a brake experiment", *J. Sound Vib.*, **331**, 5040–5053, (2012).
26. T. Butlin and J. Woodhouse, "A systematic experimental study of squeal initiation", *J. Sound Vib.*, **330**, 5077–5095, (2011).
27. A. Meziane, L. Baillet, and B. Lualagnet, "Experimental and numerical investigation of friction induced vibration of a beam-on-beam in contact with friction", *Appl. Acoust.*, **71**, 843–853, (2010).